Published in final edited form as:
Biomech Model Mechanobiol. 2011 October ; 10(5): 713–726. doi:10.1007/s10237-010-0268-9.

Experimental measurement and modeling analysis on mechanical properties of incudostapedial joint

Xiangming Zhang and
School of Aerospace and Mechanical Engineering and Bioengineering Center, University of Oklahoma, 865 Asp Avenue, Room 200, Norman, OK 73019, USA

Rong Z. Gan
School of Aerospace and Mechanical Engineering and Bioengineering Center, University of Oklahoma, 865 Asp Avenue, Room 200, Norman, OK 73019, USA

Rong Z. Gan: rgan@ou.edu

Abstract

The incudostapedial (IS) joint between the incus and stapes is a synovial joint consisting of joint capsule, cartilage, and synovial fluid. The mechanical properties of the IS joint directly affect the middle ear transfer function for sound transmission. However, due to the complexity and small size of the joint, the mechanical properties of the IS joint have not been reported in the literature. In this paper, we report our current study on mechanical properties of human IS joint using both experimental measurement and finite element (FE) modeling analysis. Eight IS joint samples with the incus and stapes attached were harvested from human cadaver temporal bones. Tension, compression, stress relaxation and failure tests were performed on those samples in a micro-material testing system. An analytical approach with the hyperelastic Ogden model and a 3D FE model of the IS joint including the cartilage, joint capsule, and synovial fluid were employed to derive mechanical parameters of the IS joint. The comparison of measurements and modeling results reveals the relationship between the mechanical properties and structure of the IS joint.

Keywords

Middle ear; Incudostapedial joint; Mechanical properties; Finite element modeling; Synovial joint

1 Introduction

The middle ear ossicular chain includes three ossicles (malleus, incus and stapes) and two joints (incudomallear and incudostapedial joints). The incudostapedial (IS) joint connects the incus to the stapes and the stapes footplate sits on the oval window and contacts to fluid inside the cochlea. The IS joint is a synovial joint consisting of a joint capsule, cartilage, and synovial fluid as observed from histology (Ohashi et al. 2005; Wang et al. 2006) and scanning electron microscopy (SEM) of the middle ear (Djeric et al. 1987; Ortug et al. 2006; Karmody et al. 2009).

Mechanical properties of the IS joint directly affect the stapes movement or the middle ear transfer function for sound transmission (Gan et al. 2004). IS joint abnormalities, such as disarticulation and ankylosis, can induce severe conductive hearing loss or even deafness

Correspondence to: Rong Z. Gan, rgan@ou.edu.

(Holler and Greenberg 1972; Suzuki et al. 2008; Sim and Chang 2008). The design and evaluation of middle ear surgery and reconstruction of the middle ear with ossicular prosthesis are also related to the structure and mechanical properties of the IS joint (Schwetschenau and Isaacson 1999; Vishwakarma et al. 2009; Celik et al. 2009).

Experimental measurement on mechanical properties of the human IS joint has never been reported in the literature because of its extremely small size and complex structure. A lack of information on the mechanical properties of the IS joint affects full understanding of middle ear biomechanics. For example, the IS joint was assumed as an isotropic elastic material in published finite element (FE) models of the human ear with a constant Young's modulus of 0.6 MPa (Prendergast et al. 1999; Wada et al. 1997; Gan et al. 2004, 2007; Gan and Wang 2007). The joint capsule, cartilage, and synovial fluid were not involved in these FE models. Funnell et al. (2005) reported on the articular connection between the incus lenticular process and stapes head using a FE model of the cat ear, but the synovial fluid was not included in the joint.

In this study, we report the experimental measurement of the mechanical properties of the human IS joint with an analytical approach and FE modeling to derive mechanical parameters of the joint. Uniaxial tension and compression, stress relaxation, and failure tests were conducted on IS joint samples in a micro-material testing system (MTS). The 3D FE model of the IS joint including the joint capsule, cartilage, and synovial fluid was created to simulate the experiment. The analytical solution was based on the hyperelastic Ogden model (Ogden 1984) and Prony series to describe mechanical behavior of the joint capsule. Finally, the comparison of measurements and FE modeling results reveals the relationship between the mechanical properties and structure of the IS joint.

2 Methods

2.1 Specimen preparation

The IS joints were harvested from eight fresh human temporal bones (5 left and 3 right) obtained through the Willed Body Program at the University of Oklahoma Health Sciences Center. The average age of donors (all male) was 62 (ranging from 53 to 82). All the experiments were performed within 6 days after harvesting the temporal bones. To maintain soft tissue compliance, the bones were immersed in 0.9% saline solution containing 15% povidone at 5°C until use. The bone was checked under the microscope to assure no degradation or abnormality before preparation of the sample. After opening the tegmen and removing the tympanic membrane together with the malleus, the temporal bone was cut into a $3 \times 3 \times 1.5$ cm^3 block to expose the IS joint with incus and stapes attached as shown in Fig. 1b. Figure 1a is a schematic showing the location of the IS joint in the middle ear.

The whole specimen was then placed on a 2D microtranslational stage in MTS (Model 100R, TestResources, MN) as shown in the experimental setup schematic (Fig. 1d). The translational stage was used for aligning the IS joint with the load cell in the vertical axis with the help of a CCD camera attached to a surgical microscope, viewing from two directions (front and side views). The stapes footplate was fixed to the bony wall using cyanoacrylate gel glue (Loctite). As validated in Cheng et al.'s studies (2007 and 2008), this kind of glue can provide sufficient fixation on the samples without noticeable dislocation happening. The other end of the IS joint, long process of the incus, was grabbed by a specially designed metal adapter, which was connected to the load cell in MTS (see pictures of the adapter in Fig. 1c). The adapter had a U-shaped groove to fit the incus with glue. Great care was taken to avoid the glue dropping onto the IS joint.

Note that the load cell's deformation was not taken into account as it had much higher stiffness than soft tissues (GPa level of load cell vs. MPa level of soft tissue). The deformation of the pedicle, which connects the incus long process and lenticular process, was also not taken into account because of its much larger elastic modulus (12 GPa, reported from Funnell et al. 2005) than that of the IS joint (MPa level).After the specimen was lined up in MTS, a preload of 0.001 N was applied to the specimen through the load cell to be settled as the initial state. This is the same method as used in our previous tests of middle ear soft tissues (Cheng et al. 2007; Cheng and Gan 2008).

2.2 Mechanical testing

The MTS with SMT-1 (10.0 Newton capacity) load cell (Interface, Inc.) was used to measure the force-displacement relation, stress relaxation function, and failure strength of the IS joint specimens. The displacement was applied to the stapes footplate, and the load cell on the top measured the force on the IS joint (Fig. 1d). In this study, the displacements recorded by MTS were used to calculate the specimen deformation. To reach the steady state for the specimen, the preconditioning was performed first on each specimen (Fung 1993). The MIS was programmed to perform 5 cycles of loading and unloading at the stretch rate of 0.025 mm/s and displacement of 0.2 mm. After preconditioning, the specimen was subjected to four tests: uniaxial tension, compression, stress relaxation, and failure tests. Note that the specimen was returned to the initial unstressed state after the tension, compression, and relaxation tests, respectively, and waited 2 min for recovery from the previous deformation. The specimen was maintained in its physiological condition by spraying normal saline solution to the specimen during the test.

2.2.1 Tension and compression tests—The dominant motion of the stapes at low frequency is a piston-like vibration under acoustic input in the ear canal (von Békésy 1960; Gyo et al. 1987), and the IS joint is subject to cyclic tension and compression. Thus, the quasi-static tension and compression tests were conducted to the specimen for measuring the stress–strain relationship of the IS joint. The tension test was performed on eight specimens at a stretch rate of 0.005 mm/s and an elongation of 0.2 mm. The compression test was performed on five specimens at a rate of 0.005 mm/s and the compressive displacement of 0.1 mm. The data recording interval was 0.2 s. Three parameters, force, displacement, and time, were recorded with a resolution level of 10^{-3} N in force and 10^{-3} mm in displacement. This data were further used to calculate the stress–strain relationship of the IS joint under tension and compression.

2.2.2 Stress relaxation test—The stress relaxation test was performed on all eight specimens to investigate the viscoelastic properties of the joint. An approximate step function of elongation was applied to the specimen at the beginning ($t = 0$) with a stretch rate of 0.4 mm/s and displacement of 0.2 mm. It took about 0.5 s to reach the peak displacement, which was small enough compared to the relaxation time (see Sect. 3). The corresponding stress including the initial stress σ_0 at $t = 0$ and relaxed stress $\sigma(t)$ were recorded over a period of time until the rate of loading change was less than 0.1 % s^{-1}, or fully relaxed. The data recording interval was 0.1 s. Then, the MTS data recording program was stopped manually, and the specimen was returned to the initial unstressed state for the failure test.

2.2.3 Failure test—The failure test was performed on all eight specimens. The stretch rate was set at 0.005 mm/s. The specimen was stretched until it was broken, and the data recording interval was 0.2 s. The entire failure process, including the force and displacement, was recorded and the breaking situation of the specimen was observed using the CCD camera.

2.3 Measurement of specimen dimensions

The IS joint is a complicated structure including the soft capsule, cartilages, and synovial fluid, and it is difficult to measure its dimensions in situ. After the completion of the failure test, the IS joint was disconnected. The incus long process, tiny pedicle, and the lenticular process were checked under the microscope carefully to assure that there was no damage on the bone. The still image of the incus lenticular process was captured using a digital CCD camera as shown in Fig. 2a. The lenticular process was placed on a horizontal plane, and the camera's angle was adjusted in a range of ±15° around the vertical direction to take at least nine images. The length a and width b of the lenticular process for each specimen were measured using the image analysis tool (Adobe Photoshop 7.0). The measurement was based on the calculation of pixels with a resolution of 50 pixels/mm or 20 μm/pixel. The largest values of a and b in perpendicular directions were accepted, and the perimeter c was calculated as $c = \pi \cdot (a+b)/2$ under the assumption that the lenticular process plate was elliptical. Table 1 lists the dimensions of the IS joint measured from eight specimens with mean and SD values. The mean values for length a, width b, and perimeter c were 0.82, 0.51, and 2.08 mm, respectively. The thickness and length of the capsule were measured based on the histology section shown in Fig. 2b from Wang et al.' paper (2006), using the same image analysis tool with 4 μm/pixel resolution. The value of 0.08 mm for capsule thickness t and 0.28 mm for length L were obtained and employed for the calculation of capsule cross-sectional area A, which was defined as the area difference between two ellipses (with capsule and without capsule) and calculated by $A = \pi \cdot [a \cdot b - (a - 2t) \cdot (b - 2t)] /4$. Table 1 lists the capsule cross-sectional area values for eight samples with a mean of 0.147 mm^2.

Note that the perimeter c and capsule cross-sectional area were calculated under the assumption that the lenticular process had an elliptical shape. This assumption was assessed by comparing the lenticular process surface area of 0.356 mm^2 obtained from sample IS1 by calculation of $\pi \times 0.84 \times 0.54/4 = 0.356$ mm^2 (formula for elliptic area) and the value of 0.348 mm^2 measured from image analysis using AutoCAD. The relative difference was about 2.2%, and the elliptical assumption was an acceptable approximation.

2.4 Analytical approach

In the uniaxial tension test, the tensile stress of the capsule, σ, was defined as the force, F, divided by the capsule cross-sectional area, A:

$$\sigma = \frac{F}{A} \tag{1}$$

and the deformation or stretch ratio of the capsule, λ, was defined as the ratio of deformed length, L, to the original length, L_0:

$$\lambda = \frac{L}{L_0} \tag{2}$$

The Ogden model (Ogden 1984) was appropriate to predict the nonlinear hyperelastic properties of middle ear soft tissues by (Cheng et al. 2007; Cheng and Gan 2008) and employed to describe the joint capsule's nonlinear mechanical properties in this study. The strain energy function W of the first order Ogden model is generally expressed as

$$W=\frac{2\mu_1}{\alpha_1^2}(\lambda_1^{\alpha_1}+\lambda_2^{\alpha_1}+\lambda_3^{\alpha_1}-3) \tag{3}$$

where λ_1, λ_2, λ_3 are three principle stretch ratios, μ_1 and α_1 are two material constants of Ogden model, and μ_1 is the initial shear modulus. Under the assumption of incompressibility of soft tissue, for uniaxial tension, the Ogden model is simplified as the stress–strain relationship,

$$\sigma=\frac{2\mu_1}{\alpha_1}\left[\lambda^{(\alpha_1-1)}-\lambda^{-(0.5_{\alpha_1}+1)}\right] \tag{4}$$

where σ is the tensile stress in Eq. (1) and λ is the stretch ratio in Eq. (2). Differentiating Eq. (4) with respect to λ, we have the elastic modulus $E(\lambda)$ as a function of λ,

$$E(\lambda)=\frac{d\sigma}{d\lambda}=\frac{2\mu_1}{\alpha_1}\left[(\alpha_1-1)\lambda^{(\alpha_1-2)}+(0.5\alpha_1+1)\lambda^{-(0.5\alpha_1+2)}\right] \tag{5}$$

Thus, two material constants (μ_1 and α_1) can be determined from the stress–stretch ratio curve of the specimen measured from the tension test through the data iteration process in MATLAB using the least-square method. Then, the constitutive equation of the IS joint capsule is derived by substituting μ_1 and α_1 into Eq. (4), and the elastic modulus of the joint is determined from Eq. (5).

Biological soft tissues usually show viscoelastic properties as the stress relaxes under constant stretch level (Fung 1993). The relaxation function $G(t)$ of the IS joint (capsule) can be expressed as the ratio of stress $\sigma(t)$ at time t with respect to the initial stress $\sigma(0)$ at $t = 0$ based on the quasi-linear viscoelastic theory (Fung 1993). To simulate the stress relaxation function $G(t)$ of the IS joint, we used the two-term Prony series,

$$G(t)=\frac{\sigma(t)}{\sigma(0)}=1-p_1(1-e^{-t/\tau_1})-p_2(1-e^{-t/\tau_2}) \tag{6}$$

where τ_1 and τ_2 are the Prony relaxation time constants, p_1 and p_2 are the first Prony constants, and $(1-p_1-p_2)$ represents the ratio between the relaxed stress and the initial stress (Li et al. 2006; Van Loocke et al. 2008). These four coefficients, τ_1, τ_2, p_1, and p_2, were determined from the measured stress relaxation curve for each specimen.

2.5 Finite element modeling

The mechanical behavior of the IS joint under different loading conditions (e.g., compression) and the effects of experimental setup and IS joint structure (cartilage and fluid) on measurement of joint mechanical properties cannot be derived using the analytic approach. Using FE modeling, we can simulate the experiment by creating a 3D FE model of the IS joint including the stapes head, lenticular process, cartilages, joint capsule, and synovial fluid. Figure 3a shows the 3D FE model of the IS joint and Fig. 3b shows the vertical (along *Z*-axis) cross-section view of the model created in ANSYS (ANSYS Inc., Canonsburg, PA). The transverse cross-section ($X-Y$ plane) of the model was simulated in an elliptical shape. The cartilages covering the surfaces of the lenticular process and stapes head had a long axis length $a = 0.82$ mm and short axis length or width $b = 0.51$ mm (not shown in the figure) based on the mean value of eight specimens from Table 1. The length *L*

and thickness *t* of the soft capsule were 0.28 and 0.08 mm, respectively, based on the histology section measurement of Fig. 2b as mentioned in the previous section. The thickness of the cartilage layer *h* covering the lenticular process or stapes head was assumed as 0.08 mm, and the depth of the synovial fluid *D* was assumed as 0.12 mm based on the histology section measurement. The effects of geometric dimensions of the cartilage and fluid viscosity are discussed in the Sect. 4.

The FE model was meshed with a total of 29,640 hexahedral elements. The bony lenticular process and stapes head and the cartilages were assigned as linear elastic Solid 45 elements in ANSYS. The capsule was assigned as nonlinear Solid 185 elements with hyperelastic and viscoelastic material properties. The synovial fluid was meshed as Fluid 80 elements. The material properties used for these components except the capsule were cited from the published data and listed in Table 2 (Fung 1993;Funnell et al. 2005;Sasada et al. 1979;Gan et al. 2004;Gan and Wang 2007). The Young's modulus of 14.1 GPa was used for the bony structure (incus and stapes head). This value was reported by Herrmann and Liebowitz (1972) first and employed in the human ear FE model by Gan et al. (2004) and Gan and Wang (2007). This value is among the range of recent results of 16 ± 3 GPa on rabbit ossicles by Soons et al. (2010).

As the first attempt to model the IS joint, the cartilage was considered as linear elastic material with Young's modulus of 10 MPa, the same value as that used by Funnell et al. (2005). The capsule was assumed as the Ogden model with two material constants, μ_1 and α_1. The values listed in Table 2 were determined by fitting the FE model-derived force-displacement curves with the experimental results in tension tests obtained in this study (see Sect. 3). The tensile or compressive force was applied at the lenticular process, and the base of the stapes head was clamped completely. Note that in tension test, the adhesive force on the contact surface between fluid and cartilage was not taken into account, and the *Z*-axial displacement was not coupled. In the compression test, the *Z*-axial displacement at the contact surface between fluid and cartilage was coupled because of the compressive force.

3 Results

Figure 4a shows the tensile force-displacement curves for loading and unloading obtained from one IS joint specimen, IS7. The hysteresis loop was observed for all specimens with the unloading curve below the loading curve. In this study, the mechanical properties of the IS joint were derived from the loading curves. Fig. 4b shows the force-displacement curves of all eight specimens (thin solid lines). The maximum displacement was set at 0.2 mm while the force was ranged from 0.190 to 0.314 N. The force-displacement curves of the IS joint show clear nonlinearity under the tension test. The variation among curves might be due to the differences of sample's age, sex, health, uncertainty of the geometric parameters, and post-mortem effects. The mean tensile force-displacement curve with SD (thick solid line with square symbols) of eight specimens is shown in Fig. 4b with a mean force of 0.262 ± 0.039 N at 0.2 mm of elongation.

The tensile force-displacement curve obtained from the FE model (thick dashed red line) is also shown in Fig. 4b. The Ogden material parameters μ_1 and α_1 for joint capsule in FE model were determined by minimizing the difference between the experimental and model-derived force-displacement curves using the least-square method. It was found that using the values of $\mu_1 = 0.0985$ MPa and $\alpha_1 = 9.12$ (listed in Table 2) the FE model-derived force-displacement curve was very close to the mean curve of the experimental data. Thus, the FE model can predict mechanical behavior of the IS joint in tension very well.

Figure 5a shows the stress–stretch ratio curves for all eight specimens (thin solid lines). The specimens (capsules) were stretched up to λ about 1.7, and the maximum stress was ranged from 1.47 to 2.31 MPa. The mean stress–stretch ratio curve with an SD (thick solid line with square symbols) is also shown in Fig. 5a. The mean maximum stress was 1.86 MPa with an SD of 0.24 MPa. The absolute SD increased with increasing stress. All the stress–stretch curves in Fig. 5a were used to derive Ogden model constants μ_1 and α_1 using Eq. (4) and the data iteration process in MATLAB. The first two rows in Table 3 list μ_1 and α_1 values for eight specimens with the mean and SD μ_1 was from 0.0758 to 0.165 MPa with a mean of 0.104 MPa; α_1 was from 7.84 to 10.05 with a mean of 9.13. The correlation coefficients between the Ogden material constants and all stress–stretch curves were over 0.997, which proved that the Ogden model well represented nonlinearity of joint capsule's stress–strain relationship. For the mean stress–stretch ratio curve in Fig. 5a, μ_1 was determined as 0.102 MPa and α_1 as 9.18. Thus, the mean constitutive equation of the IS joint capsule obtained from tensile experiments was

$$\sigma = 0.0222 \times (\lambda^{8.18} - \lambda^{-5.59})\ \text{MPa} \tag{7}$$

The elastic modulus-stretch ratio relationship was then obtained by substituting $\mu_1 = 0.102$ and $\alpha_1 = 9.18$ into Eq. (5):

$$E(\lambda) = 0.0222 \times \left[8.18 \times \lambda^{7.18} + 5.59 \times \lambda^{-6.59}\right]\ \text{MPa} \tag{8}$$

which was plotted in Fig. 5b (thick solid line). The elastic modulus changed from 0.30 to 8.92 MPa when the stretch ratio increased from 1 to 1.72.

The dashed red line with square symbols in Fig. 5b represents the FE model-derived elastic modulus-stretch ratio curve. Using the Ogden constants listed in Table 2 for capsule, the FE model derived elastic modulus of the capsule at a stretch ratio of 1.72 was 8.34 MPa, which was 6.5% smaller than that of analytical results.

Figure 6a shows the compressive force-displacement curves for loading and unloading obtained from IS joint specimen IS7, the same specimen as that in Fig. 4a. Compared with Fig. 4a, a larger hysteresis loop was observed in the compression test. This may suggest that more energy was dissipated during the loading and unloading cycle in compression than in tension. Figure 6b shows the force-displacement curves (thin solid lines) of five specimens (no compression test on the first three specimens). The maximum compressive displacement was set at 0.1 mm while the force was ranged from 0.354 to 0.676 N, much larger than the tensile force observed in Fig. 4b. The variation of these curves was due to individual difference among the specimens. The results show that the compressive force-displacement relations of all specimens are nonlinear, similar to the tension results. However, the force in compression was much larger than that recorded in the tension test at the same displacement, which could be caused by involvement of the synovial fluid and cartilages in compression. The mean force-displacement curve with SD was also shown in Fig. 6b. The mean value of compressive force increased to 0.505 N with the displacement increasing to 0.1 mm. The absolute SD increased with the displacement increasing while the relative SD remained stable at around 25%. The relative SD in compression tests was larger than that in tension tests (Fig. 4b). This may be caused by more components involved in compression with more complicated deformation.

The compressive force-displacement curve obtained from the FE model (thick dashed red line) is also displayed in Fig. 6b. The model-derived force at displacement of 0.1 mm was

0.411 N, which was 18.6% smaller than the mean value of measurement results (0.505 N). However, the curve was still within the range of experimental curves and was 16.1% larger than the smallest value of 0.354 N at 0.1 mm displacement. It is noticeable that the FE-derived curve was very close to the experimental curves on specimen IS7. The results in Fig. 6b demonstrate that the FE model of the IS joint is able to predict the mechanical behavior of the IS joint in compression.

Figure 7a shows the normalized stress relaxation function $G(t)$ measured from eight specimens. The relaxation function decreased with time and finally reached a stable state after 200 s. The mean stress relaxation function $G(t)$ is shown in Fig. 7b with SD. The Prony series of Eq. (6) was used to describe the relaxation function for each individual sample. Through the data iteration in MATLAB based on the eight curves in Fig. 7a, the Prony constants p_1, p_2, τ_1, and τ_2 were derived and listed in Table 3 with mean values and SDs. p_1 was ranged from 0.229 to 0.498 with a mean of 0.392, p_2 from 0.079 to 0.232 with a mean of 0.140, τ_1 from 0.81 to 1.95 s with a mean of 1.30 s, and τ_2 from 14.06 to 73.04 s with a mean of 46.07 s. Using the mean values of p_1, p_2, τ_1, and τ_2, the relaxation function $G(t)$ was finally obtained as

$$G(t)=1-0.4\times(1-e^{-t/1.59})-0.129\times(1-e^{-t/36.95}) \tag{9}$$

Note that in stress relaxation tests, the ramp load process (displacement 0.2 mm with initial stretch rate 0.4 mm/s) was used to simulate the step function approximately. Considering that the loading time of 0.5 s was quite smaller than the relaxation time τ_1, and τ_2, the stress relaxation function derived from the tests was accepted as an approximation of the real relaxation function of the IS joint.

The failure tensile force, stress, displacement, and stretch ratio obtained from eight specimens are listed in Table 4. The failure force varied from 0.259 to 0.713 N with a mean value of 0.465 N and SD of 0.164 N. The failure stress varied from 1.81 to 4.68 MPa with a mean of 3.19 MPa and SD of 1.15 MPa. The failure displacement ranged from 0.249 to 0.330 mm with a mean of 0.291 mm and SD of 0.034 mm. The failure stretch ratio ranged from 1.89 to 2.18 with a mean value of 2.04 and SD of 0.12. The failure stretch ratio had relatively smaller variation among different specimens than that of the failure stress. The joint capsule usually broke gradually from one side to another side, and the breaking area generally started at the middle of the capsule. Figure 8 shows the broken status of the joint from two specimens (IS4 and IS8).

4 Discussion

4.1 Tension test versus compression test

The IS joint presented quite different properties in tension and compression tests as observed from the experiments. In compression, the IS joint sustained much larger force than that in tension test when the displacement was the same. This difference may be caused by involvement of the synovial fluid and cartilages. Due to the complicated deformation shape and multiple components, there is no simple analytical solution for the compression test. The FE model became the best choice to study the deformation behavior of the IS joint in tension and compression. Figure 9a shows the FE model-derived deformation shape (in $X-Z$ plane) and Z-axial displacement distribution of the IS joint under tensile force. The force applied at the lenticular process was 0.20 N, and the displacement was 0.184 mm. As mentioned in the previous Sect. 2.5, the Z-axial displacements of the fluid and cartilage were not coupled together and the fluid had almost no contribution to sustain the tensile force. The bones (incus lenticular process and stapes head) and cartilages had very little deformation. The

average Green strain components of selected capsule element (located at the middle region of the capsule as shown in Fig. 9a) are $E_Z = 0.557$, $E_X = -0.375$, and $E_{XZ} = 0.004$. The shear strain is much smaller than the normal strain and can be neglected. Thus, the capsule soft tissue can be considered under pure tension except the boundary area near the junction to the bone.

Figure 9b shows the deformation shape (in $X-Z$ plane) and Z-axial displacement distribution of the IS joint under compression. The compressive force applied on the incus lenticular process was 0.20 N, the same as that applied in tension test, and the displacement was −0.069 mm. The bone, cartilage, fluid, and capsule together as a structure were involved in the compression. The force applied on the bone (lenticular process) was transferred into the pressure in fluid, and the fluid was squeezed from the center to sides and created pressure on the capsule. Not like the pure tension, the capsule in compression suffered different deformations: the compression directly from the lenticular process and the bending induced by fluid pressure. The average Green strain components of the same capsule element as that in tension are $E_Z = -0.108$, $E_X = -0.145$, and $E_{XZ} = -0.680$. The shear strain here is much higher than in the tension test. The cartilages show noticeable deformations compared to the tension test. The strain E_Z in cartilage was almost evenly distributed and had a mean value around −0.109. The joint structure deformation under compression induced smaller displacement than in the tension test under the same force (0.069 vs. 0.185 mm) as visualized in Fig. 9. The differences of compression from the tension test were probably caused by two factors: (1) the different deformation mode of joint capsule (nearly pure tension versus compression plus bending); (2) the involvement of fluid and cartilage in compression. The contributions of the cartilage and fluid to the IS joint mechanics in compression are discussed in the following section.

4.2 Effects of cartilage and synovial fluid on compression

As discussed in the earlier section, the cartilage and synovial fluid in the IS joint play an important role in compression. We did realize that there were some difficulties to get accurate dimension for the cartilage thickness, h, and the synovial fluid depth, D as shown in Fig. 3b. Moreover, the thickness of cartilage may not distribute evenly. The elastic modulus for the cartilage employed in the model of 10 MPa was from normal human articular cartilage not from IS joint cartilage. The elastic modulus of IS joint cartilage has not been reported and may have certain difference from 10 MPa. The viscosity of synovial fluid used in this study, 0.4 $N \cdot s/m^2$, was from other human joint not from IS joint. Thus, the effects of cartilage and fluid geometry, the elastic modulus of the cartilage, and the viscosity of synovial fluid on the IS joint compression were evaluated in FE model as follows.

1. Cartilage and fluid geometry effects. The length of the capsule, L ($L = 2 \times h + D$, see Fig 3b), was kept constant while h and D changed. Two cases were studied: (1) control case where $h = 80$ μm and $D = 120$ μm; and (2) $h = 40$ μm and $D = 200$ μm. Figure 10a shows the compressive force-displacement curves derived from the FE model with different cartilage thickness and fluid depth. The force at displacement of 0.1 mm in case 2 was 0.361 N, 12.1% smaller than the value of the control case, 0.411 N. The results indicate that smaller cartilage thickness decreased the IS joint's ability to sustain compressive force.
2. Cartilage elastic modulus effect. Three values of cartilage modulus were employed in the FE model: 10 MPa (control case), 5 and 20 MPa. Figure 10b shows the compressive force-displacement curves with three cartilage elastic moduli. The force at displacement of 0.1 mm was 0.387 N when the cartilage elastic modulus was 5 MPa. This force was 5.7% smaller than that of the control case (0.411 N). The force at displacement of 0.1 mm increased to 0.429 N when the cartilage

elastic modulus was 20 MPa. This force was 4.4% larger than that of the control case. The cartilage elastic modulus did effect the IS joint mechanics in compression, but it was less significant compared to the cartilage thickness effect. The change of cartilage thickness also induced the change of boundary and load conditions of the capsule, while cartilage elastic modulus only changed itself. This may also cause the difference between these two factors' effects on compression.

3. Synovial fluid viscosity effect. Two viscosity values were employed in the FE model: 0.4 $N \cdot s/m^2$ (control) and 0.1 $N \cdot s/m^2$ (reduced). The stretch rate in the FE model was set to the same value as the experiments, 0.005 mm/s. Figure 10c shows the compressive force-displacement curves derived from FE model with these two viscosities of fluid. The results indicate that the fluid viscosity did not have a noticeable effect on the quasi-static test with a low strain rate.

4.3 Off-axial force effect on experimental measurement

The force applied to the incus lenticular process during the experiment might not coincide perfectly with the central axis of the IS joint, and tilting of the lenticular process could occur. To estimate the effect of off-axial force on experimental measurement, 0.25 N force was applied at the lenticular process with 0.2 mm offset from the central axis of the IS joint in the FE model. The force-displacement curves were derived for both tension and compression cases. Figure 11a shows the deformation shape and distribution of the *Z*-axial displacement of the IS joint under off-axial tensile force (the deformation under compression not shown). φ is the tilting angle between the lenticular process and $X-Y$ plane. Figure 11b shows the tensile force-displacement curve derived from the control and off-axial loading from the model in comparison with the mean experimental curve from Fig. 4b. When the force reached 0.25 N, the off-axial displacement of the node where the force was applied was 0.211 mm, 7.1% larger than the control displacement, which was 0.197 mm and the tilting angle φ was 11.3°. Figure 11c shows the compressive force-displacement curve derived from the control and off-axial cases from the model in comparison with the mean experimental curve from Fig. 6b. When the force reached 0.40 N, the off-axial displacement was 0.104 mm, 6.3% larger than the on-axial displacement of 0.098 mm, and φ was 8.7°. These results indicate that the off-axial force does not affect the force-displacement relations significantly, and the experimental results in both tension and compression tests had better agreement with the control modeling results than the off-axial results. Thus, the error induced by the off-axial load in experimental setup was limited and can be neglected reasonably.

It is noticed that in experiments, the load was applied at the end of incus long process and transferred through the pedicle onto the lenticular process, which may induce bending on the pedicle. To estimate the deformation and bending angle of the pedicle, the pedicle was simplified as a cantilever with one end fully clamped with lenticular process and the other end applied with bending moment of 0.25×0.2 N · mm. The pedicle length was approximately assumed as 0.32 mm and the cross-section was assumed as 0.11×0.48 mm^2 based on the histology section image and the data used in Funnell et al.'s study (2005) (doubled the value of the cat pedicle). 12 GPa was used as the elastic modulus for pedicle, which was the same as that used by the Funnell et al. study. The maximum bending angle and flexibility at the end of the pedicle were obtained from the FE model as 3.220 and 0.0111 mm. These values were relatively smaller than that of the IS joint deformation. Thus, the effect of the pedicle on FE modeling results was not taken into account in this study.

4.4 Contributions of this work and future studies

This study is the first report on mechanical properties of the human incudostapedial (IS) joint. The IS joint was considered as a synovial joint with fluid inside and capsule

surrounding. The relationship between the structure and mechanical behavior of the joint was analyzed under tensile and compressive forces. The hysteresis and stress relaxation observed from the joint specimens demonstrate that the IS joint has typical viscoelastic properties. The IS joint also presents nonlinear hyperelastic properties for which the Ogden model was employed to analyze the mechanical behavior of the joint capsule. Two material constants, μ_1 and α_1, were determined based on experimental measurements. These parameters are valuable to be used in the FE model of the human ear under static pressure, such as that reported by Wang et al. (2007). The nonlinear hyperelastic properties of ear tissues are critical for developing the FE model-derived tympanogram, which may have potential for clinical application in diagnosis of middle ear disease in relation to structure disorders.

In this study, the quasi-static mechanical properties of human IS joint were obtained from tension, compression, and failure tests. While the IS joint works over the auditory frequency range (20–20,000 Hz), its dynamic properties or complex modulus under high frequency is important for understanding the middle ear function. The dynamic properties of some middle ear soft tissue, such as the TM, have been reported by Luo et al. (2009). However, the frequency-dependant mechanical properties of the IS joint have not been reported and need to be investigated in our future study. Moreover, although the viscosity of synovial fluid has no significant effect on static or quasi-static mechanics, the dynamic behavior of the joint should have relation with the synovial fluid viscosity. Thus, the viscosity effect on IS joint dynamic mechanics needs further studies.

3D kinematics of middle ear ossicles have a close relation with the IS joint mechanical properties. The motion of the ossicular chain has been studied through experimental measurements (Decraemer and Khanna 1995, 2000; Decraemer and Khanna 2004) and modeling analysis (Eiber 1999; Mills et al. 2004; Funnell et al. 2005; Gan and Wang 2007; Gan et al. 2007; Homma et al. 2009). However, in these published FE models, the IS joint was assumed as a solid elastic block and it is not clear what the effect of IS joint synovial structure on the ossicular motion and middle ear transfer function is. How does the application of the synovial IS joint bring us new knowledge in middle ear mechanics? To answer these questions, the FE model of the synovial IS joint reported in this study can be added into the comprehensive FE model of human ear previously reported by Gan and Wang (2007); Gan et al. (2007). It is expected that the accuracy of 3D motion of the ossicles and middle ear transfer function will be improved through future FE modeling.

5 Conclusions

The mechanical properties of the human IS joint were studied through experimental measurements and FE modeling analysis. The uniaxial tension, compression, relaxation, and failure tests were conducted in joint samples using the MTS. An FE model of the IS joint including the bones, cartilages, synovial fluid, and joint capsule was created to simulate the experiments. The hyperelastic Ogden model was employed to describe the nonlinear behavior of the joint capsule. The results demonstrate that the IS joint is a viscoelastic structure with nonlinear stress–strain relationship. The IS joint sustains higher force in compression than in tension. This behavior was caused by the different deformation modes under tension and compression and was contributed by synovial fluid and cartilages. The effects of off-axial force, geometry and elastic modulus of cartilages, and viscosity of fluid on experimental measurements were evaluated using the FE model.

Acknowledgments

The authors thank Wei Li, M. S., former graduate student in our biomedical engineering lab at the University of Oklahoma, and Don Nakmali BSEE at Hough Ear Institution for their expert technical assistance on human

temporal bone preparation. This work was supported by NIH/NIDCD R01DC006632 and NSF/CMMI-0510563 grants.

References

Celik H, Felek SA, Islam A, Demirci M, Samim E, Oztuna D. The impact of fixated glass ionomer cement and springy cortical bone incudostapedial joint reconstruction on hearing results. Acta Otolaryngol. 2009; 19:1–6.

Cheng T, Dai C, Gan RZ. Viscoelastic properties of human tympanic membrane. Ann Biomed Eng. 2007; 35(2):305–314. [PubMed: 17160465]

Cheng T, Gan RZ. Mechanical properties of anterior malleolar ligament from experimental measurement and material modeling analysis. Biomech Model Mechanobiol. 2008; 7(5):387–394. [PubMed: 17710457]

Decraemer W, Khanna S. Malleus vibration modelled as rigid body motion. Acta Otorhinolaryngol Belg. 1995; 49(2):139–145. [PubMed: 7610906]

Decraemer, WF.; Khanna, SM. Measurement, visualization and quantitative analysis of complete three-dimensional kinematical data sets of human and cat middle ear. In: Gyo, K.; Wada, H., editors. Middle ear mechanics in research and otology. Singapore: World Scientific; 2004. p. 3-10.

Decraemer, WF.; Khanna, S. New insights into vibration of the middle ear. The Netherlands: Kugler Publications, The Hague; 2000.

Djeric D, Savic D, Polic D. A scanning electron microscopic study of the incudostapedial joint. Rev Laryngol Otol Rhinol (Bord). 1987; 108(5):463–466. [PubMed: 3444994]

Eiber A. Mechanical modeling and dynamic behavior of the human middle ear. Audiol Neurootol. 1999; 4:170–177. [PubMed: 10187926]

Fung, YC. Biomechanics: mechanical properties of living tissues. 2nd edn.. New York: Springer; 1993.

Funnell WR, Heng ST, McKee MD, Daniel SJ, Decraemer WF. On the coupling between the incus and the stapes in the cat. J Assoc Res Otolaryngol. 2005; 6(1):9–18. [PubMed: 15735938]

Gan RZ, Feng B, Sun Q. Three-dimensional finite element modeling of human ear for sound transmission. Ann Biomed Eng. 2004; 32(6):847–859. [PubMed: 15255215]

Gan RZ, Wang X. Multifield coupled finite element analysis for sound transmission in otitis media with effusion. J Acoust Soc Am. 2007; 122(6):3527–3538. [PubMed: 18247761]

Gan RZ, Reeves BP, Wang X. Modeling of sound transmission from ear canal to cochlea. Ann Biomed Eng. 2007; 35(12):2180–2195. [PubMed: 17882549]

Gyo K, Aritomo H, Goode RL. Measurement of the ossicular vibration ratio in human temporal bones by use of a video measuring system. Acta Otolaryngol (Stockh). 1987; 103(1–2):87–95. [PubMed: 3564932]

Herrmann, G.; Liebowitz, H. Mechanics of bone fractures. In: Liebowitz, H., editor. Fracture: an advanced treatise. New York: Academic Press; 1972. p. 772-840.

Holler FC, Greenberg LM. Incudostapedial joint disarticulation. Arch Otolaryngol. 1972; 95(2):182–184. [PubMed: 5060068]

Homma K, Du Y, Shimizu Y, Puria S. Ossicular resonance modes of the human middle ear for bone and air conduction. J Acoust Soc Am. 2009; 125(2):968–979. [PubMed: 19206873]

Karmody CS, Northrop CC, Levine SR. The incudostapedial articulation: new Concepts. Otol Neurotol. 2009 (Epub. ahead of print).

Li ZP, Alonso JE, Kim JE, Davidson JS, Etheridge BS, Eberhardt AW. Three-dimensional finite elementmodels of the human pubic symphysis with viscohyperelastic soft tissues. Ann Biomed Eng. 2006; 34(9):1452–1462. [PubMed: 16897423]

Luo H, Dai C, Gan RZ, Lu H. Measurement of Young's modulus of human tympanic membrane at high strain rates. J Biomech Eng. 2009; 131(6):064501–064508. [PubMed: 19449971]

Mills R, Szymanski M, Abel E. Movements of the intact and reconstructed ossicular chain during changes in static pressure. Acta Otolaryngol. 2004; 124(1):26–29. [PubMed: 14977074]

Ogden, R. Non-linear elastic deformations. Chichester: Ellis Harwood Ltd.; 1984.

Ohashi M, Sawaguchi A, Ide S, Kimitsuki T, Komune S, Suganuma T. Histochemical characterization of the rat ossicular joint cartilage with a special reference to stapediovestibular joint. Acta Histochem Cytochem. 2005; 38(6):387–392.

Ortug G, Ortug C, Aydar Y. Configurations of incudostapedial joint surface, an SEM study. Faseb J. 2006; 20(4):A442.

Prendergast PJ, Ferris P, Rice HJ, Blayney AW. Vibroacoustic modeling of the outer and middle ear using the finite-element method. Audiol Neurootol. 1999; 4(3–4):185–191. [PubMed: 10187928]

Sasada T, Tsukamoto Y, Mabuchi K, Morita M, Kondo H. Viscosity of synovial-fluid. Biorheology. 1979; 16(6):494.

Schwetschenau EL, Isaacson G. Ossiculoplasty in young children with the Applebaum incudostapedial joint prosthesis. Laryngoscope. 1999; 109(10):1621–1625. [PubMed: 10522932]

Sim RJ, Chang P. Incudostapedial ankylosis from temporomandibular joint disruption. Otolaryngol Head Neck Surg. 2008; 139(1):166–167. [PubMed: 18585584]

Soons JA, Aernouts J, Dirckx JJ. Elasticity modulus of rabbit middle ear ossicles determined by a novel micro-indentation technique. Hear Res. 2010; 263(1–2):33–37. [PubMed: 19818840]

Suzuki M, Kanebayashi H, Kawano A, Hagiwara A, Furuse H, Yamaguchi T, Shimizu M. Involvement of the incudostapedial joint anomaly in conductive deafness. Acta Otolaryngol. 2008; 128(5):515–519. [PubMed: 18421604]

Van Loocke M, Lyons CG, Simms CK. Viscoelastic properties of passive skeletal muscle in compression: stress-relaxation behaviour and constitutive modelling. J Biomech. 2008; 41(7): 1555–1566. [PubMed: 18396290]

Vishwakarma R, More YI, Joseph ST, Patel KB, Ramani MK, More RI. Incudostapedial joint arthroplasty using temporalis fascia/perichondrium ties. Am J Otolaryngol. 2009; 30(3):171–175. [PubMed: 19410122]

von Békésy, G. Experiments in hearing. New York: McGraw-Hill Book Company; 1960.

Wada, H.; Metoki, T.; Kobayashi, T. Three-dimensional finite-element method (FEM) analysis of the human middle ear. In: Huttenbrink, KB., editor. Middle ear mechanics in research and otosurgery Dresden University of technology. Germany: Dresden; 1997. p. 76-80.

Wang H, Northrop C, Burgess B, Liberman MC, Merchant SN. Three-dimensional virtual model of the human temporal bone: a stand-alone, downloadable teaching tool. Otol Neurotol. 2006; 27(4): 452–457. [PubMed: 16791035]

Wang X, Cheng T, Gan RZ. Finite-element analysis of middle-ear pressure effects on static and dynamic behavior of human ear. J Acoust Soc Am. 2007; 122(2):906–917. [PubMed: 17672640]

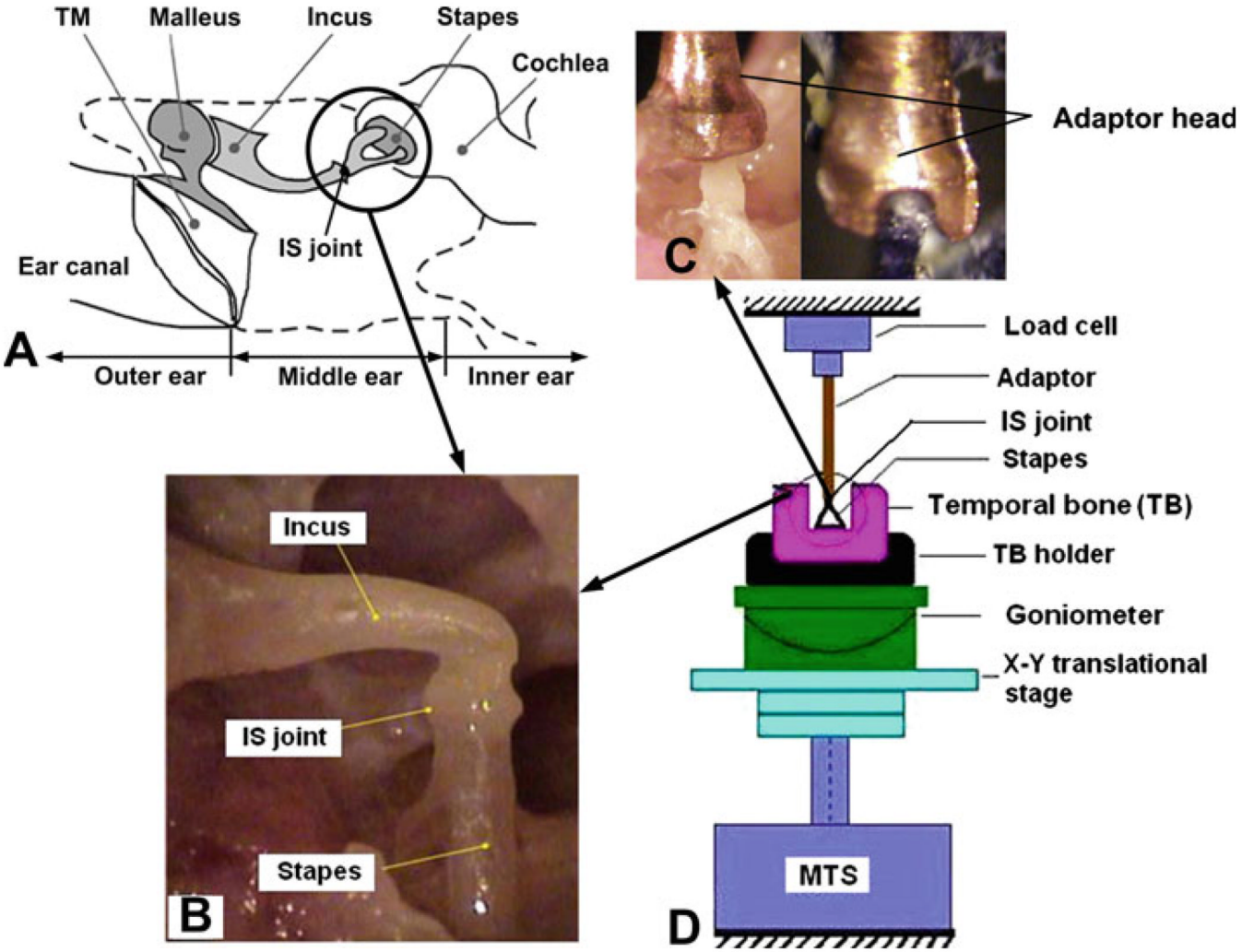

Fig. 1.

a A schematic showing the location of the IS joint in the middle ear. **b** A picture of a human IS joint specimen with incus and stapes attached. **c** Two views of the specially designed metal adapter for gripping the IS joint specimen. **d** Schematic of the experiment setup for IS joint testing in MTS. The IS joint specimen was placed in a 2D micro-translational stage on MTS. The stapes was fixed on the temporal bone and the incus long process was attached to the metal adaptor. The specimen was lined by adjusting the translational stage with the help of a CCD camera attached to a surgical microscope

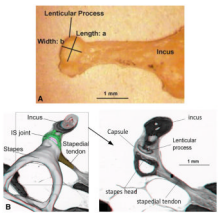

Fig. 2.

a Image of the incus and lenticular process taken from a specimen. *a* and *b* represent the length and width of the lenticular process surface, respectively. **b** Image of the histology section of the human middle ear (Wang et al. 2006) used to measure the length and thickness of the IS joint capsule

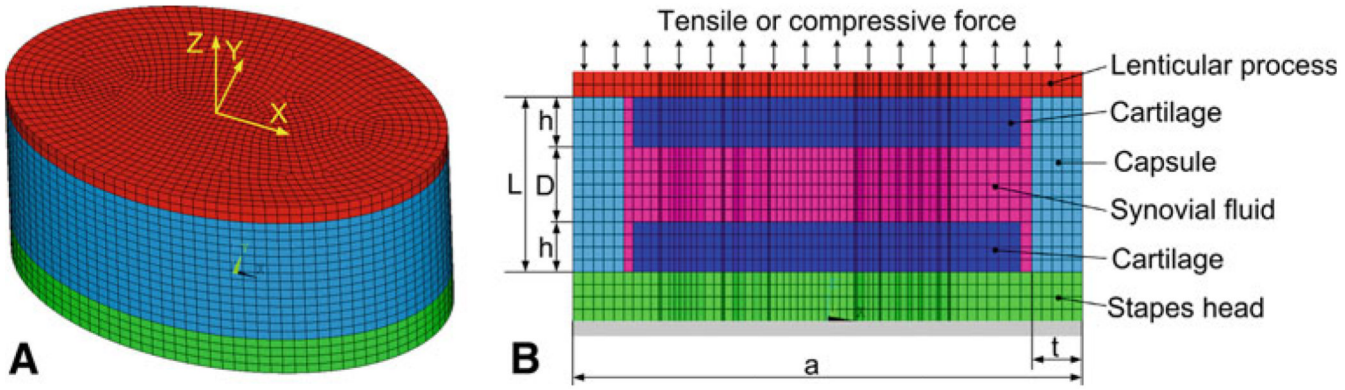

Fig. 3.

a 3D FE model of the IS joint with the lenticular process (*top, red*), capsule (*middle, blue*) and stapes head (*bottom, green*). The transverse cross-section (*X*−*Y* plane) of the IS joint was modeled as an ellipse. **b** Axial cross-section (*X*−*Z* plane) of the FE model with lenticular process, cartilage, synovial fluid, capsule, and stapes head. The force was applied perpendicularly to the surface of lenticular process and the base of the stapes head was fully clamped

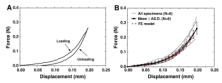

Fig. 4.

a The force-displacement curves of specimen IS7 obtained under loading and unloading in the uniaxial tension test. **b** The force-displacement curves of eight specimens under loading process (*thin solid line*) with the mean curve and SD (*thick solid line with square symbols*) and the FE model-derived curve (*thick dashed line*)

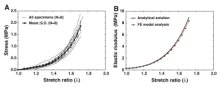

Fig. 5.

a The stress–stretch ratio curves of eight specimens (*thin solid line*) with the mean curve and SD (*thick solid line with square symbols*) obtained from tension tests. **b** The elastic modulus-stretch ratio curve obtained from Eq. (5) with the experimental mean data of μ_1 = 0.102 MPa and α_1 = 9.18 for the capsule (thick solid line) and the FE model-derived elastic modulus-stretch ratio curve with μ_1 = 0.0985 MPa and α_1 = 9.12 listed in Table 2 (*dashed line with square symbols*)

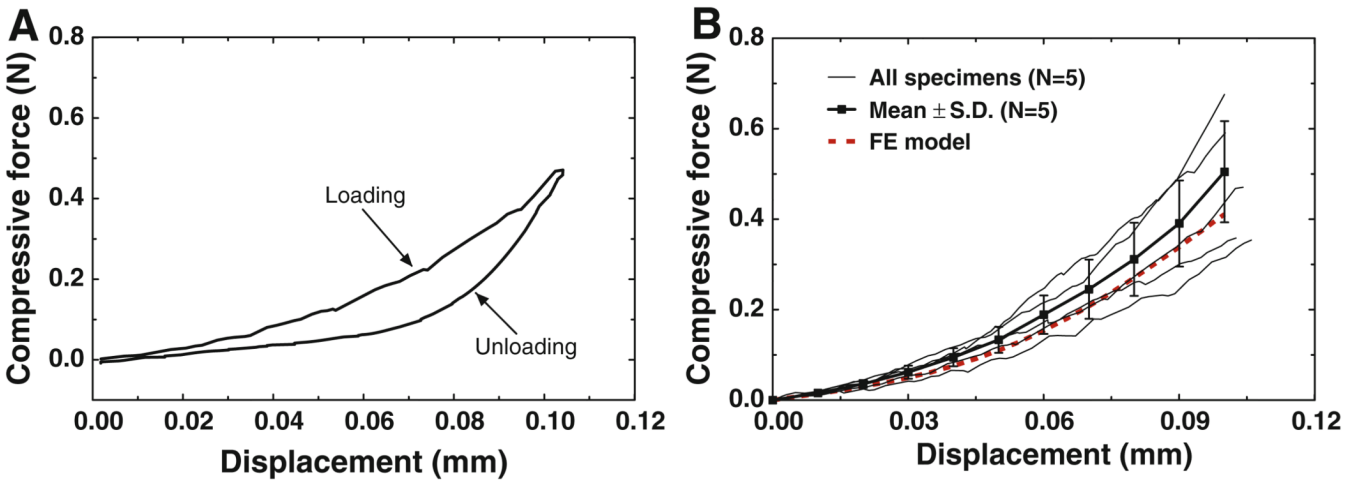

Fig. 6.

a The force-displacement curves of specimen IS7 obtained under loading and unloading in the compression test. **b** The force-displacement curves of five specimens from the compression tests (*thin solid line*) with the mean curve and SD (*thick solid line with square symbols*) and the FE model-derived curve (*thick dashed line*)

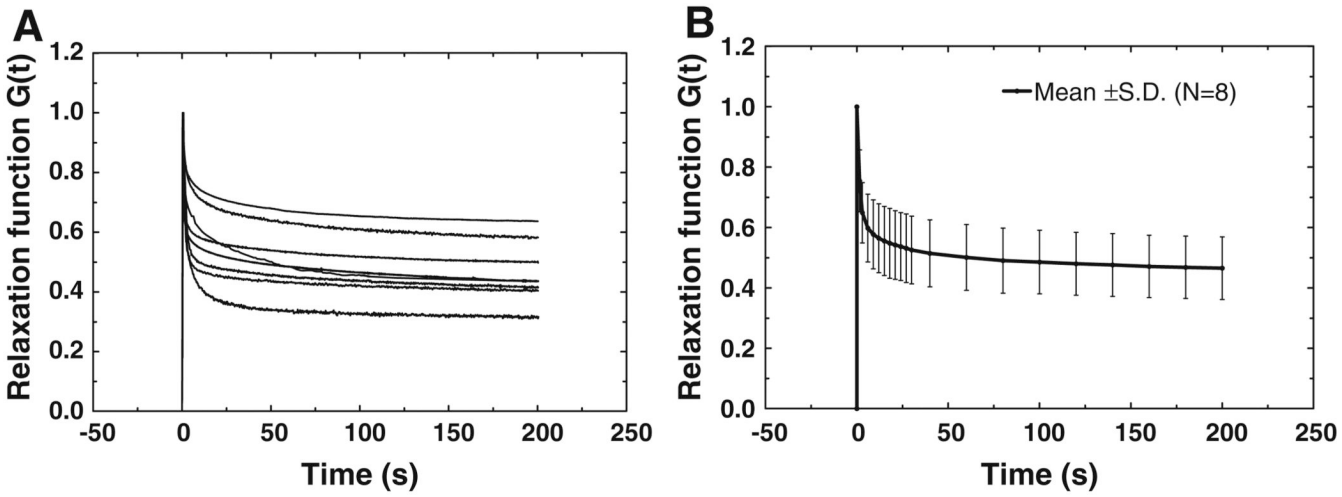

Fig. 7.

a Normalized stress relaxation function $G(t)$ curves measured from eight IS joint specimens.

b The mean curve of stress relaxation function $G(t)$ of eight specimens with SD

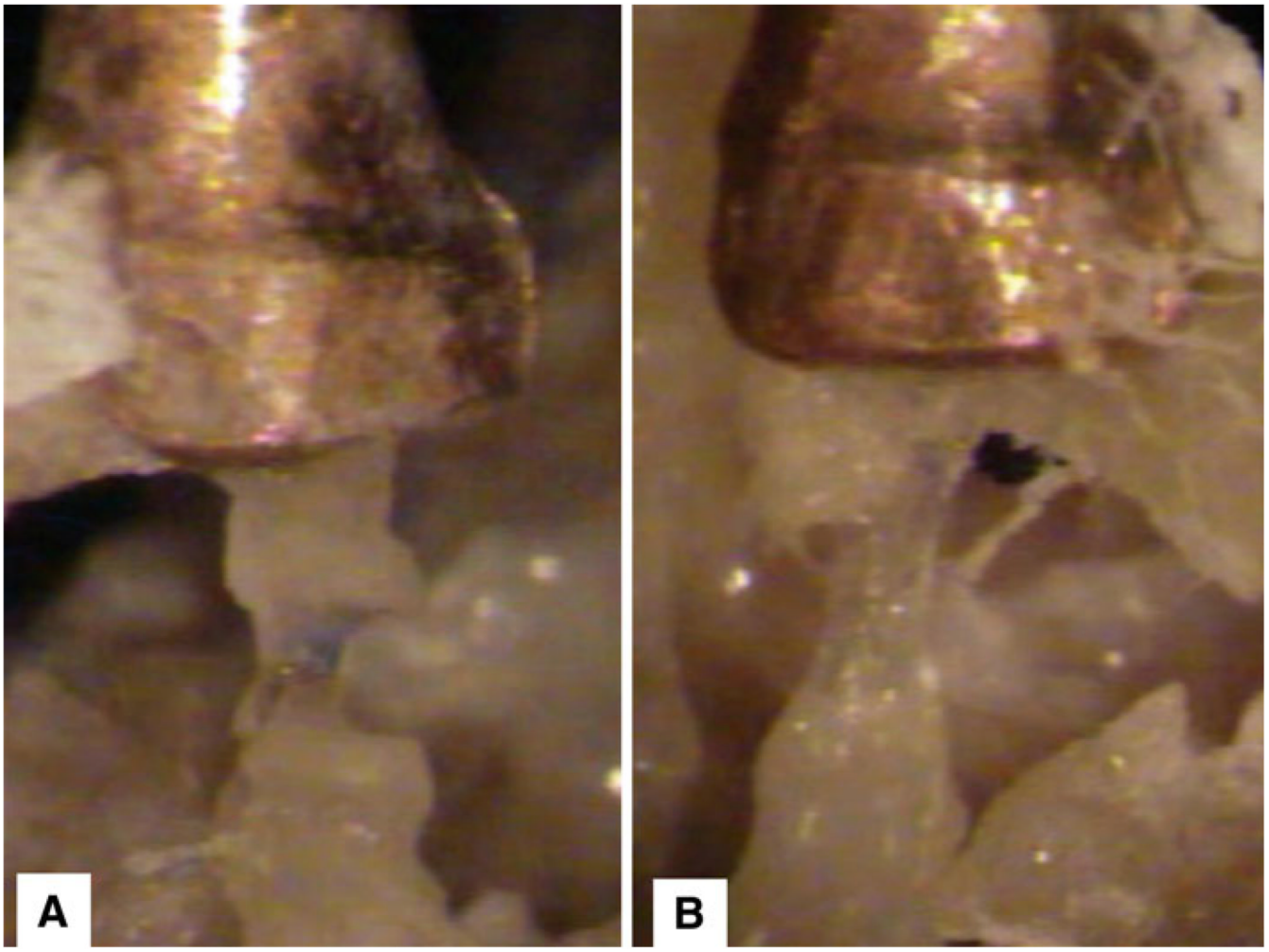

Fig. 8.
Pictures of the broken status of the joint from two specimens in failure tests. **a** Specimen IS4; **b** Specimen IS8

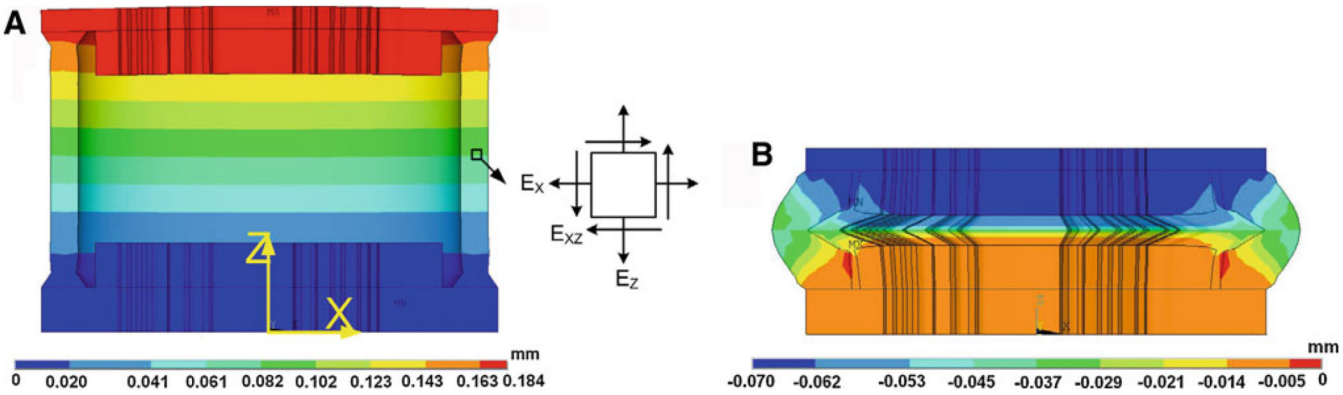

Fig. 9.

a The FE model-derived deformation shape (in $X-Z$ plane) with Z-axial displacement distribution of the IS joint under tensile force 0.20 N (fluid not shown). The maximum displacement was 0.184 mm at the lenticular process (*top* surface). **b** FE model-derived deformation shape and Z-axial displacement distribution of the IS joint under compressive force 0.20 N. The displacement was −0.069 mm at the lenticular process. An element at the center of the capsule was selected to study the Green strain tensor under tension and compression

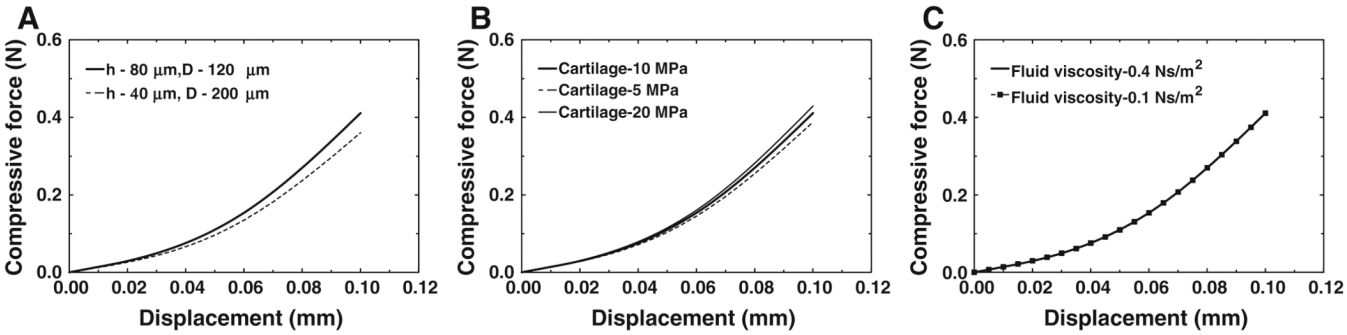

Fig. 10.

a Compressive force-displacement curves derived from the FE model with different cartilage thickness. **b** Compressive force-displacement curves derived from the FE model with different elastic modulus of cartilage. **c** Compressive force-displacement curves derived from the FE model with different viscosity of synovial fluid

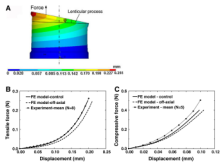

Fig. 11.

a The deformation shape and *Z*-axial displacement distribution of the IS joint under off-axial tensile force (0.2 mm offset from the central axis). φ is the tilting angle between the lenticular process and *X*−*Y* plane. **b** Comparison of force-displacement curves in tension derived from the control (co-axial), off-axial FE model and experimental mean. **c** Comparison of force-displacement curves in compression derived from the control, off-axial FE model and experimental mean

Table 1

Dimensions of the IS joint specimens

IS joint specimen	IS1	IS2	IS3	IS4	IS5	IS6	IS7	IS8	Mean	SD (±)
Length: *a* (mm)	0.84	0.88	0.86	0.76	0.80	0.76	0.82	0.80	0.82	0.04
Width: *b* (mm)	0.54	0.58	0.56	0.50	0.50	0.44	0.50	0.48	0.51	0.04
Perimeter: *c* (mm)	2.17	2.29	2.22	1.98	2.04	1.89	2.07	2.01	2.08	0.13
Capsule cross area: *A* (mm^2)	0.153	0.163	0.158	0.138	0.143	0.131	0.146	0.141	0.147	0.011

Table 2

Components and mechanical parameters of the IS joint

Components	Young's modulus (Pa)	Poisson's ratio	Viscosity (Ns/m^2)
Incus	1.41×10^{10}	0.3	
Stapes head	1.41×10^{10}	0.3	
Cartilage	1.00×10^{7} (Funnell et al. 2005)	0.3	
Capsule	Ogden model ($m_1 = 98500$ Pa, $a_1 = 9.12$)		
Synovial fluid	2.20×10^{9} (Bulk modulus)		0.4 (Fung 1993; Sasada et al. 1979)

If not specially noted, the parameters are from Gan and Wang (2007); Gan et al. (2007)

Table 3

Ogden model and Prony series constants of IS joint specimens determined from tension and relaxation tests

	IS1	IS2	IS3	IS4	IS5	IS6	IS7	IS8	Mean	SD (±)
m_1(MPa)	0.117	0.0897	0.0758	0.124	0.0896	0.0920	0.0810	0.165	0.104	0.030
α_1	9.11	9.10	9.49	8.42	10.05	9.27	9.71	7.84	9.13	0.71
P_1	0.325	0.229	0.498	0.431	0.469	0.514	0.397	0.271	0.392	0.106
$\tau_{1(s)}$	1.03	1.43	1.95	1.52	0.95	0.91	0.81	1.83	1.30	0.44
P_2	0.232	0.132	0.090	0.132	0.207	0.079	0.101	0.146	0.140	0.055
$\tau_{2(s)}$	33.22	40.09	73.04	57.58	14.06	48.66	48.95	52.97	46.07	17.51

Table 4

Failure force, displacement, stress, and stretch ratio of the IS joint capsule

	IS1	IS2	IS3	IS4	IS5	IS6	IS7	IS8	Mean	SD (±)
Failure force (N)	0.713	0.393	0.448	0.514	0.259	0.464	0.267	0.660	0.465	0.164
Failure displacement (mm)	0.249	0.319	0.330	0.269	0.260	0.260	0.319	0.319	0.291	0.034
Failure stress (MPa)	4.66	2.41	2.83	3.72	1.81	3.54	1.83	4.68	3.19	1.15
Failure stretch ratio (λ)	1.89	2.14	2.18	1.96	1.93	1.93	2.14	2.14	2.04	0.12